

1
2 **Melting relations in the system FeCO₃-MgCO₃ and thermodynamic**
3 **modeling of Fe-Mg carbonate melts**
4

5 **Nathan Kang^{a,*}, Max W. Schmidt^a, Stefano Poli^b, James A. D. Connolly^a and Ettore**
6 **Franzolin^a**

7
8 ^a Department of Earth Sciences, Institute of Geochemistry and Petrology, ETH,
9 Clausiusstrasse 25, 8092 Zurich, Switzerland

10 ^b Dipartimento di Scienze della Terra, Università degli Studi di Milano, Via Botticelli 23,
11 20133 Milano, Italy

12 * Corresponding author. Tel.: +41 44 63 23789. E-mail: nathan.kang@erdw.ethz.ch (N.Kang)

13
14 **ABSTRACT**

15 To constrain the thermodynamics and melting relations of the siderite-magnesite (FeCO₃-
16 MgCO₃) system, 27 piston cylinder experiments were conducted at 3.5 GPa and 1170-
17 1575 °C. Fe-rich compositions were also investigated with 13 multi anvil experiments at 10,
18 13.6 and 20 GPa, 1500-1890 °C. At 3.5 GPa, the solid solution siderite-magnesite coexisting
19 with melt over a compositional range of $X_{Mg} (=Mg/(Mg+Fe_{tot})) = 0.38-1.0$, while at ≥ 10 GPa
20 solid solution appears to be complete. At 3.5 GPa the system is pseudo-binary because of the
21 limited stability of siderite or liquid FeCO₃, Fe-rich carbonates decomposing at subsolidus
22 conditions to magnetite-magnesioferrite solid solution, graphite and CO₂. Similar reactions
23 also occur with liquid FeCO₃ resulting in melt species with ferric iron components, but the
24 decomposition of the liquid decreases in importance with pressure.

25 At 3.5 GPa the metastable melting temperature of pure siderite is located at 1264 °C whereas
26 pure magnesite melts at 1629 °C. The melting loop is non-ideal on the Fe-side where the
27 dissociation reaction resulting in Fe³⁺ in the melt depresses melting temperatures and causes a
28 minimum. Over the pressure range of 3.5-20 GPa, this minimum is 20-35 °C lower than the
29 (metastable) siderite melting temperature. By merging all present and previous experimental
30 data, standard state (298.15 K, 1 bar) thermodynamic properties of the magnesite melt
31 (MgCO₃L) end-member are calculated and the properties of (Fe,Mg)CO₃-melt fit by a regular
32 solution model with an interaction parameter of -7600 J/mol. The solution model reproduces
33 the asymmetric melting loop and predicts the thermal minimum at 1240 °C near the siderite
34 side at X_{Mg}=0.2 (3.5 GPa). The solution model is applicable to pressures reaching to the
35 bottom of the upper mantle and allows calculation of phase relations in the FeO-MgO-O₂-C
36 system.

37 *Keywords:* siderite; magnesite; experimental petrology; melting relations; oxidation; solution
38 model

39 **1. Introduction**

40 The stability of carbonates against decarbonation and melting is of considerable interest for
41 understanding the global carbon cycle (Dasgupta and Hirschmann 2010). Carbon solubilities
42 in mantle silicates are low, typically a few ppm and at most 10-20 ppm (Keppler et al. 2003,
43 Shcheka et al. 2006, Panero and Kabbes 2008). Hence, carbon is likely to be stored in a
44 separate phase either oxidized as carbonate(s), carbonated fluids (as documented e.g. in
45 inclusions in diamonds; Wang et al. 1996, Stachel et al. 2000, Klein-BenDavid et al. 2009) or
46 melts or in reduced phases such as diamonds, carbides or Fe-C alloys (Boulard et al. 2012).
47 Computed phase equilibria on sediment bulk compositions and metabasalts as well as phase
48 equilibria experiments on carbonated sediments, basaltic eclogites and peridotites suggest that
49 Ca-Mg-Fe carbonates remain stable beyond arc-depths and enter the deeper parts of the

50 mantle with higher melting temperatures than typical modern subduction geotherms (Wallace
51 and Green 1988, Falloon and Green 1989, Yaxley and Green 1994, Molina and Poli 2000,
52 Kerrick and Connolly 2001, 2001b, Dasgupta et al. 2004, Yaxley and Brey 2004, Dasgupta
53 and Hirschmann 2006, Poli et al. 2009, Mann and Schmidt 2015). At depth greater than 4-5
54 GPa, experiments indicate that magnesite (MgCO_3) is the most stable carbonate (Biellmann et
55 al. 1993, Fiquet et al. 2002, Isshiki et al. 2004). In general, carbonates tend to have high X_{Mg}
56 values compared to coexisting Fe-Mg silicates; typical compositional ranges for peridotites
57 are $X_{\text{Mg}}^{\text{magnesite-siderite}}$ of 0.93-0.99 (Brey et al. 2008, Brey et al. 2009, Ghosh et al. 2009), for
58 metabasalts 0.67-0.82 (Dasgupta et al. 2004, Yaxley and Brey 2004, Dasgupta et al. 2005), for
59 metapelites 0.3-0.8 (Thomsen and Schmidt 2008, Grassi and Schmidt 2011) and 0.2-0.9 in
60 carbonatites (Buckley and Woolley 1990). Hence, there is ample reason to investigate the Fe-
61 rich side of the magnesite-siderite binary experimentally and to develop a thermodynamic
62 model for the solid and liquid solutions in this system.

63 At the extreme Fe-rich end, natural siderite is generally associated with ankerite
64 $(\text{Ca,Fe})\text{CO}_3$ in sedimentary banded iron formations (BIFs; Klein 2005, Kholodov and
65 Butuzova 2008). Before the rise of oxygen ~2.3 Ga ago, BIFs and anoxic shales were not only
66 platform sediments but also abundant on deep ocean floors (Beukes and Gutzmer 2008), but
67 most of the deep deposits have disappeared from the Earth surface via subduction (Polat et al.
68 2002, Dobson and Brodholt 2005). High pressure devolatilization and melting in such Fe-rich
69 systems are poorly understood and experimental investigation of the MgCO_3 - FeCO_3 system is
70 required to understand the fate of subducted C-bearing BIFs. Siderite also occurs in
71 hydrothermal veins, in extraterrestrial materials such as on Mars (Morris et al. 2010), in the
72 Martian meteorite ALH84001 (Eiler et al. 2002) and in altered igneous rocks.

73 The melting of pure siderite is stable above 6.8 GPa (Tao et al. 2013, Kang et al. 2015), the
74 melting of pure magnesite above 2.5 GPa (Irving and Wyllie 1975). At lower pressures
75 magnesite simply decomposes to $\text{MgO}+\text{CO}_2$ while siderite decomposition involves a redox

76 reaction to magnetite and graphite. Due to the discordance of the graphite-CO₂ (CCO) oxygen
77 buffer with the common Fe-buffers (iron-wustite, wustite-magnetite, and magnetite-hematite),
78 wustite+CO₂ only become stable at temperatures higher than siderite stability (Fig. 1).

79 Experimental studies on the subsolidus phase relations in the MgCO₃-FeCO₃ system at 0.2-
80 0.4 GPa, 350-550 °C (Rosenberg 1967), at 1.5 GPa, 600-800 °C (Goldsmith et al. 1962) and
81 at 3.5 GPa, 900-1100 °C (Franzolin et al. 2011) prove that there is continuous solid solution
82 between siderite and magnesite. Subsolidus phase relations were then thermodynamically
83 modeled within the ternary Ca-Mg-Fe carbonate system at high pressures (Davidson 1994,
84 Franzolin et al. 2011, Holland and Powell 2011). The binary MgCO₃-FeCO₃ has recently been
85 studied at 6 GPa and 900-1700 °C (Shatskiy et al. 2015a), where results suggest minor
86 incongruent melting of Mg-Fe-carbonate to form oxide-carbonate liquids coexisting with CO₂
87 fluid. Phase equilibria studies, in particular on compositions near Fe-endmembers are
88 complicated by the fact that at conditions above the iron-wustite buffer, some of the ferrous
89 iron always oxidizes to ferric iron.

90 This study defines the melting loop of the MgCO₃-FeCO₃ binary at 3.5 GPa, 1170-1575 °C,
91 filling a decisive gap on the melting behavior of iron-bearing carbonates at mantle conditions.
92 In addition, we present experimental data constraining the Fe-rich side of this binary at 10,
93 13.6, and 20 GPa. Based on the experimental data we fit the thermodynamic solution model
94 for Mg-Fe carbonate melts considering the influence of fO₂ and redox reactions of iron-
95 bearing phases. This melt model provides the first approximation for the prediction of Mg-Fe
96 carbonate melting relations at pressure.

97 **2. Experimental and analytical methods**

98 *2.1 Starting materials*

99 Starting materials were prepared from natural magnesite with an X_{Mg} of 0.989 from
100 Obersdorf (Philipp 1998), synthetic magnesite (99.9% MgCO₃ powder from Alfa-Aesar) and

101 synthetic siderite. Starting materials for piston cylinder experiments were mixtures of natural
102 magnesite and synthetic siderite, while synthetic magnesite was used in the multi-anvil
103 experiments. Magnesite was dried at 220 °C for ~16 h and then stored at 110 °C. Siderite was
104 synthesized from iron oxalate, sealed into gold capsules of 5.4 mm outer diameter, at 350 °C
105 and 200 MPa in an externally heated cold seal vessel run for 6 days (French 1971). The
106 synthetic siderite had a gray-white, slightly brownish color. Each newly synthesized siderite
107 batch was analyzed by scanning electron microscope and X-ray diffraction, which did yield
108 pure siderite. Siderite was stored at ambient temperature in an evacuated glass desiccator to
109 slow oxidation, but with time develops a more intensive brown color due to oxidation. Storing
110 siderite at e.g. 110 °C in a vacuum oven to prevent hydration led to more rapid oxidation.
111 Drying siderite is not suitable as it starts to oxidize at 110 °C, hence our starting materials
112 may have contained small amounts of moisture. To minimize absorbed H₂O and oxidation,
113 siderite was synthesized repeatedly as required and experiments were done in less than 2
114 months after synthesis. Magnesite and siderite were mixed under alcohol and after drying, the
115 starting mixtures (Table 1) were stored in a glass desiccator under vacuum.

116 *2.2 Experimental methods*

117 High pressure experiments were conducted in an end-loaded piston cylinder at 3.5 GPa and
118 in a 1000 ton Walker-type multi-anvil at 10, 13.6 and 20 GPa. Piston cylinder experiments
119 were run with Teflon foil-talc-pyrex-graphite-MgO assemblies. To avoid Fe-loss to metal
120 capsules and prevent the consequent oxidation of the sample, inner graphite capsules were
121 inserted into 3 mm O.D. Pt capsules, which were welded shut. Run temperatures were
122 controlled by Eurotherm controllers within ± 2 °C, using B-type (Pt₉₄Rh₆/Pt₇₀Rh₃₀)
123 thermocouples. The assembly was gradually decompressed after quenching the experiments
124 by turning off the heating power.

125 Multi-anvil experiments were performed employing tungsten carbide cubes with truncation
126 edge lengths of 11, 8 and 3.5 mm in combination with prefabricated Cr₂O₃-doped MgO-
127 octahedra of 18, 14 and 10 mm edge length (18/11 assembly for 10 GPa, 14/8 for 13.6 GPa
128 and 10/3.5 for 20 GPa). Assemblies were composed of stepped (18/11, 14/8) or straight
129 (10/3.5) LaCrO₃ heaters, ZrO₂ sleeves, internal MgO spacers and an molybdenum end ring
130 and disc. The starting materials were loaded directly into Au₈₀Pd₂₀ capsules stacked in the
131 central part of the furnace assembly. The 18/11 and 14/8 assemblies contained axial
132 thermocouples while the 10/3.5 assembly has a thermocouple running across the center of the
133 furnace (Stewart et al. 2006). Temperature was controlled using a B-type (Pt₉₄Rh₆/Pt₇₀Rh₃₀)
134 thermocouple for 10 and 13.6 GPa or C-type (W₉₅Re₅-W₇₄Re₂₆) for 20 GPa. Typical thermal
135 gradients across a capsule are 15-25 °C in 18/11 and 14/8 assemblies. Temperature gradients
136 within the 10/3.5 assembly are 30-50 °C over the capsule length of 1.2 mm. Quenching was
137 done by turning off the heating power and was followed by pressure unloading for about 15-
138 20 h.

139 *2.3 Analytical techniques*

140 Capsules were mounted longitudinally in epoxy resin and polished to the center. The open
141 capsules were repeatedly impregnated in low-viscosity resin to avoid mechanical loss of the
142 exposed phases. Experimental charges were analyzed with a JEOL JXA8200 electron
143 microprobe (EPMA) to determine phase compositions. Hematite (Fe₂O₃) and periclase (MgO)
144 have been used as standards for Fe and Mg. The quenched melt was measured at 15 kV
145 acceleration voltage and 6 nA with a beam diameter of 15-20 μm to minimize beam damage.
146 Counting times were 30 s on the peak and 15 s on the background. Note that melt pools with
147 small melt fractions interstitial to grain boundaries were extremely difficult to measure,
148 especially with a defocused electron beam, and contamination by adjacent mineral phases
149 during the measurement could not always be excluded. In such cases we used an SEM-EDX

150 that allows acquisition using polygonal area measurements. CO₂ contents of carbonate melts
151 were estimated by difference of the totals to 100. These estimates were within a few percent
152 of the expected stoichiometric value with respect to (Mg,Fe²⁺)CO₃. Nevertheless, the
153 quenched melt may contain holes or disperse graphite, thus influencing analytical totals.
154 Secondly, the carbonate melts probably contain a small ferric component, and thirdly they
155 may dissolve molecular CO₂, both leading to CO₂-values different from those of
156 (Mg,Fe²⁺)CO₃. Calculated CO₂-concentrations were only used to plot liquid compositions in
157 FeO-MgO-CO₂ projected from graphite.

158 High resolution back-scattered electron (BSE) images were obtained from a Jeol JSM
159 6390LA scanning electron microscope to study textural relationships between phases. Micro-
160 Raman spectroscopy (Horiba Jobin Yvon LabRam HR 800) was employed to identify the
161 nature of the oxide phases (spinel group vs magnesiowustite). After analysis all samples were
162 stored in a desiccator.

163 **3. Experimental results**

164 Altogether, 40 successful experiments were performed on 6 different bulk compositions at
165 3.5, 10, 13.6 and 20 GPa, and at temperatures between 1170 and 1890 °C. All experimental
166 run conditions, phase assemblages and their molar compositions are presented in Table 1.
167 Distinctive textural features of the experimental charges at subsolidus and melting conditions
168 at 3.5 GPa and at higher pressure are shown in Figs. 2 and 3.

169 *3.1 Equilibration and run textures*

170 For the supersolidus experiments, 5-20 minutes runtime were sufficient to attain textural
171 equilibrium. Enhanced by high temperatures and the presence of a liquid phase, equilibrium is
172 evidenced by triple junctions, homogenous phase compositions, completely reacted starting
173 materials and pronounced grain growth of subsolidus carbonates. In general, equilibrium
174 carbonates form discrete large polyhedral grains. The onset of partial melting in experiments

175 is detected using textural criteria. Mostly, the liquid migrates and collects in the warmer zone
176 of the capsule. At low melt fractions, interstitial melt pools along grain edges (Fig. 2d) or
177 concentration of melt along capsule walls are observed (Fig. 2b, c). The carbonate melts are
178 not quenchable, quench phases from the liquid consist of dendritic aggregates of carbonates
179 (Carb-q, Fig. 2b, c, d, f) intergrown with iron oxides. Where large enough, these quench
180 oxides have been identified by Raman spectroscopy as magnetite (Mt-q), indicating that the
181 melt contains a minor ferric component.

182 For the subsolidus experiments, textural and compositional equilibrium was more difficult
183 to reach, generally requiring ≥ 1 -2 h runtime. Disequilibrium was indicated by irregular grain
184 shapes (Fig. 2a), magnesite-rich mineral cores and compositionally zoned carbonates. The only
185 result that is used from the subsolidus experiments are the carbonate compositions, assuming
186 that the measured carbonate compositions are (meta)stable at run condition.

187 Bubbles indicating gas- or fluid-saturation were rarely observed (Figs. 2, 3), also not in the
188 capsules where considerable equilibrium magnetite formed through reaction (1). In the
189 subsolidus runs, this may indicate that the copious amounts of CO₂ resulting from reaction (1)
190 were contained in the porosity of the graphite capsule, in supersolidus experiments all of the
191 CO₂ may be dissolved in the melt. The latter is also indicated by the coexistence of three Fe-
192 Mg phases + graphite, the phase rule only allowing for four phases in this system. Regarding
193 oxygen fugacity, the graphite-CO₂ buffer hence represents only an upper limit, supersolidus
194 experiments with all CO₂ dissolved in the melt may have a reduced CO₂-activity and hence an
195 oxygen fugacity slightly below CCO.

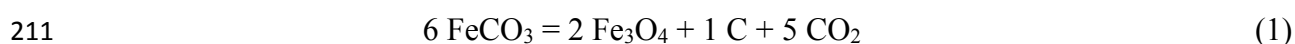
196

197 *3.2 Auto-redox dissociation, decarbonation and metastable equilibrium*

198 All textural and chemical features of the melting experiments in Pt-C double capsules at
199 3.5 GPa indicate equilibrium, however, this equilibrium is at least in part metastable.
200 Metastable equilibria can be experimentally investigated at appropriate run durations,

201 profiting of transition phases governed by intermediate steps of minima in the free energy
202 surface, according to the Ostwald step rule (see Putnis, 1992). Metastable equilibrium melting
203 of mullite has been extensively investigated in the system $\text{Al}_2\text{O}_3 - \text{SiO}_2$ at room pressure (see
204 Pask, 1996 for a review), and of muscovite in the system $\text{K}_2\text{O}-\text{Al}_2\text{O}_3-\text{SiO}_2-\text{H}_2\text{O}$ (Rubie and
205 Brearley, 1990; Brearley and Rubie, 1990) at 0.1 GPa, revealing that metastable liquids can
206 persist over geologic timescales.

207 The range of compositions on the join magnesite-siderite for which metastable melting
208 occurs cannot be predicted a priori; as a consequence run durations were optimized following
209 a trial and error procedure. Initial run times were 24 hours, but had to be shortened to 5-20
210 min in order to minimize auto-redox dissociation of the siderite component:

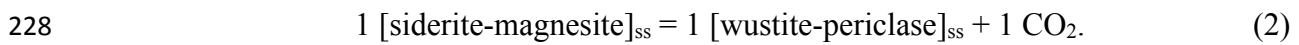


212 (French 1971, Weidner 1972, Koziol 2004, Tao et al. 2013, Kang et al. 2015). This reaction
213 progresses slowly with time, shifting the composition of the coexisting solid and liquid
214 carbonate phases towards the Mg-side. At least part of the resulting ferric iron and probably
215 most of the CO_2 are dissolved in the melt. Our results indicate that supersolidus experiments
216 equilibrate almost instantly (5-20 minutes) while subsolidus experiments result in polygonal
217 textures with 120° triple junction after 1-2 hours. However, run durations of 1-2 hours in the
218 supersolidus led to extensive redox-dissociation in Fe-rich compositions rendering the choice
219 of the optimal run duration difficult. Experiments directly run in $\text{Au}_{80}\text{Pd}_{20}$ capsules resulted in
220 minor Fe^0 -loss causing a slightly stronger net oxidation of the charge.

221 *3.3 The siderite-magnesite join at 3.5 GPa*

222 The most critical compositions of run products at 3.5 GPa (Table 1) are depicted in 10
223 isothermal triangular sections (Fig. 4) saturated in graphite. The compositions of the
224 experimental carbonate liquid and solid pairs are shown in an isobaric T-X diagram (Fig. 5) of
225 the siderite-magnesite join. Unfortunately, this system is generally characterized by either the

226 auto redox dissociation (1) of the siderite component and/or the simple decarbonation reaction
227 of siderite-magnesite solid solution:



229 The oxide phases are composed of large and idiomorphic grains (up to $\sim 100 \mu\text{m}$),
230 identified as magnetite-magnesioferrite solid solution ($(\text{Mg},\text{Fe}^{2+})\text{Fe}^{3+}_2\text{O}_4$) or magnesiowustite
231 ($(\text{Mg},\text{Fe}^{2+})\text{O}$). As argued below, the experiments are most likely not on the CCO (C-CO-CO₂)
232 oxygen fugacity buffer, lending support to the hypothesis that the CO₂ produced by reactions
233 (1) and (2) may completely dissolve in the melt.

234 The textures and compositions of the experimental run products were used to define the
235 liquidus and solidus phase boundaries between carbonate liquid (Liq) and solid (Carb_{ss}). Bulk
236 and phase compositions are expressed on a molar basis i.e. $X_{\text{Mg}} = \text{Mg}/(\text{Fe}_{\text{tot}}+\text{Mg})$ (Table 1).
237 Subsolidus phase assemblages change considerably at different bulk X_{Mg} . The amount of
238 magnetite-magnesioferrite solid solution (Mt_{ss}) in the run products increases with Fe content
239 in the bulk. At temperatures of 1170-1230 °C and bulk X_{Mg} of 0.1-0.15, crystal aggregates are
240 dominantly composed of Mt_{ss} and little carbonate (Fig. 2a). Some of the initial experiments
241 (e.g. L-7 and L-8) exhibit large almost unreacted magnesite (X_{Mg} of ~ 0.94 -0.98) grains up to
242 $\sim 180 \mu\text{m}$; in subsequent experiments, care was taken to grind the starting materials to $< 10 \mu\text{m}$
243 grain size. Experiments with Pt-C double capsules do not inhibit completely the auto-redox
244 dissociation (1) and decarbonation reaction (2) of the siderite component, even with short run
245 times (5 min, Fig. 2d, e, f). Experimental products at subsolidus conditions with bulk
246 $X_{\text{Mg}}=0.2$ -0.4 have Carb_{ss} and Mt_{ss}. At higher bulk X_{Mg} the run products had magnesiowustite
247 (Mwu_{ss}) as the dominant oxide phase, its abundance generally increasing with run duration
248 (Fig. 2c) and temperature. Subsolidus phase assemblages with a bulk X_{Mg} of 0.75 appear at
249 temperatures up to $\sim 1380 \text{ }^\circ\text{C}$. These experimental charges contain mostly crystal aggregates
250 of $(\text{Fe},\text{Mg})\text{CO}_3$ and very minor oxide phases, either Mt_{ss} or Mw_{ss} or both.

251 Solid phase assemblages do not invariably include oxide phases, e.g. where first partial
252 melting of carbonates occurs at 1250 °C with bulk X_{Mg} of 0.2, crystals consist essentially of
253 $Carb_{ss}$ (Fig. 2b). Carbonate melt is recognized by dendritic intergrowth of carbonate and oxide
254 quench fractions. The measured melt compositions range from $X_{Mg} = 0.212$ to 0.826.
255 Experiments with a higher bulk X_{Mg} of 0.75 show the onset of partial melting from ~1400 °C
256 upwards, these experimental charges are characterized by some minor unavoidable Mt_{ss} (Fig.
257 2d). Complete melting is obtained at 1575 °C (Fig. 2f).

258 *3.4 The Fe-rich side of the $MgCO_3$ - $FeCO_3$ join at 10 – 20 GPa*

259 Additional melting experiments were performed with the starting compositions
260 $Mg_{0.1}Fe_{0.9}CO_3$ and $Mg_{0.15}Fe_{0.85}CO_3$, to define the Fe-rich side of the siderite-magnesite join at
261 10, 13.6 and 20 GPa. Textural features of experimental charges and compositions of run
262 products are summarized in Figs. 3 and 6, experimental data of the pure siderite component
263 are from Kang et al. (2015).

264 The experimental charges from 10-20 GPa are mostly partially molten at temperatures
265 from 1500 to 1890 °C, at 1550 °C one experiment (SM-05) contains only polygonal carbonate
266 crystals, indicating subsolidus conditions. Similar to the experiments at 3.5 GPa, Mg-bearing
267 siderite melt forms a dendritic texture composed of carbonate quench commonly accompanied
268 with small Fe-rich oxide quench phases (Fig. 3d). In some experiments melt is a more
269 homogenous carbonate quench showing only minor or no oxide quench (Fig. 3b, c).

270 The near-solidus experiments are characterized by wide melting intervals spanning 170 °C
271 at 10 GPa, 100 °C at 13.6 GPa and 320 °C at 20 GPa, but over most of these intervals, melt
272 proportions are small and do not exceed 5-15 vol% (Fig. 3b). We explain the appearance of a
273 small melt fraction, increasing little with temperature over a large temperature interval by
274 either absorbed water in the starting material or H_2O resulting from hydrogen diffusion
275 through the capsule wall during the experiment. We hence interpret the solidus of the dry

276 system to occur when large amounts (>30%) of melt appear, in particular as the Fe-rich bulk
 277 compositions melt almost congruently. In comparison to the experiments at 3.5 GPa, charges
 278 do not contain equilibrium Fe-spinel (Mt_{ss}) or magnesiowustite (Mwu_{ss}), but only a quench of
 279 Fe-oxides (magnetite) interstitial to the dendritic quench of carbonates. At all pressure
 280 condition, the compositions of the carbonates and coexisting melt phases are located towards
 281 the Fe-rich side (Fig. 6). One experiment (SM-04, 1670 °C, 10 GPa) appears to be
 282 inconsistent with all other experiments, the reason for this remains unclear.

283 4. Thermodynamics of carbonate melts in the system FeCO₃-MgCO₃

284 To derive a simple thermodynamic model for carbonate melts from our experiments we
 285 assume that the melt can be described as a binary mixture between magnesite and siderite
 286 endmember compositions, i.e., we neglect the Fe³⁺ component and dissolved CO₂ in the melt.
 287 We adopt the van Laar model (Holland and Powell 2003) of Franzolin et al. (2011) for fully
 288 disordered solid carbonate, which gives the partial molar gibbs energy of magnesite and
 289 siderite as

$$290 \quad g_i = g_i^0 + R * T * \ln(X_i) + R * T * \ln(\gamma_i) \quad (3)$$

291 where g_i^0 is the molar gibbs energy of the pure endmember, X_i its mol fraction in the solution,
 292 and the activity coefficient

$$293 \quad \ln(\gamma_i) = \frac{2 * \alpha_i * (X_j * \alpha_j)^2}{(\alpha_i + \alpha_j) * (\alpha_i * X_i + \alpha_j * X_j)^2} * W_{sol} \quad (4)$$

294 with $\alpha_{mag} = 1$ J/mol, $\alpha_{sid} = 0.01$ J/mol + 0.000666 J/mol * T, and $W_{sol} = 10000$ J/mol. For
 295 the liquid we assume a regular solution model, such that

$$296 \quad R * T * \ln(\gamma_i) = (1 - X_i)^2 * W_{liq} \quad (5)$$

297 where W_{liq} is an interaction parameter to be determined by analysis of the experimental
 298 results (Supplementary material). More complex, both subregular and assymmetric formulations

299 for the liquid resulted in models that predicted implausible phase relations. The unknown
 300 interaction parameter W_{liq} was calculated as the average of the values obtained by solving

$$g_{mag} = g_{magL}$$

$$g_{sid} = g_{sidL}$$

301 at the experimentally determined solidus conditions at 3.5 GPa and results to -7600 J/mol. For
 302 these calculations, the thermodynamic properties of the endmembers siderite (Table 2) and
 303 siderite melt (FeCO_3L) are taken from Kang et al. (2015). The caloric properties G_0 and S_0 of
 304 magnesite were adopted from (Holland and Powell 2011), whereas the volumetric data (V_0 , α_0 ,
 305 K_0 and K') are from Merlini et al. (2016). Note that the volume data of Merlini et al. (2016)
 306 are consistent with those on siderite and magnesite by Litasov et al. (2008, 2013). The
 307 endmember data for magnesite liquid (MgCO_3L) were derived from the congruent melting
 308 curve of magnesite. At pressures below 4 GPa, melting of magnesite is observed at ~ 1585 °C,
 309 3 GPa and at 1610 °C, 3.6 GPa (Irving and Wyllie 1975). At higher pressures the melting
 310 temperature of MgCO_3 is located at ~ 1910 °C, 8 GPa and 2090 °C, 15 GPa (Katsura and Ito
 311 1990). Based on these four experimental brackets, we adopt the following melting curve for
 312 pure magnesite

$$313 \quad T_m(\text{°C}) = 1292.85 + 103.82 * P - 3.38 * P^2 \quad (\text{P in GPa}).$$

314 It is assumed that the temperature dependence of the thermal expansion (α_T) and bulk
 315 modulus (K_T) of all endmembers are adequately represented by the empirical relations

$$316 \quad \alpha_T = \alpha_0 * \left(1 - \frac{10}{\sqrt{T}} \right) \quad (6)$$

$$317 \quad K_T = K_0 (1 - 1.5 * 10^{-4} (T - 298.15)) \quad (7)$$

318 given by Holland and Powell (1998) and volumes are computed from the Murnaghan equation
 319 of state

$$320 \quad V(T, P) = V(T, P_r) * \left[1 - K' * \frac{P}{\{K' * P + K(T, P_r)\}} \right]^{\frac{1}{K'}} \quad (8)$$

321 The heat capacity of magnesite is adjusted at high temperatures (>2000 K) such that C_P
322 converges to the Dulong-Petit limit

$$323 \quad C_P = 3 * R * n + \alpha_T^2 * V_T * K_T * T \quad (9)$$

324 where R is the gas constant and n the number of atoms in the substance of interest. The C_P of
325 magnesite at low temperatures (< 800 K) was computed from Holland and Powell (2011). The
326 total heat capacity range $C_P(T)$ is then fitted adopting the following polynomial (Holland and
327 Powell 1998)

$$328 \quad C_P = a + b * T + \frac{c}{T^2} + \frac{d}{\sqrt{T}} \quad (10)$$

329 The equilibrium condition, $G^{MgCO3} = G^{MgCO3L}$ on the melting curve was then used to solve for
330 H_0 , S_0 , V_0 , α_0 , and K_0 of $MgCO_3L$. The pressure derivative of the bulk modulus K' for the melt
331 is set to the same value as for the solid, i.e. $K'(\text{melt}) = K'(\text{solid}) = 5$. The thermodynamic data
332 of all end-members are presented in Table 2.

333 5. Discussion

334 5.1 The siderite-magnesite melting loop and pure siderite melting

335 The experimental data and the calculated melting loop in the $FeCO_3$ - $MgCO_3$ system at 3.5
336 GPa are illustrated in Fig. 5. At 3.5 GPa, only considering the binary siderite-magnesite solid
337 and liquid solutions, our model predicts an asymmetric melting loop (grey field) with both the
338 solid and melt side having a negative deviation from ideal behavior and a thermal minimum at
339 X_{Mg} of 0.2 and ~1240 °C. The exact location and temperature of this minimum is a result of
340 the thermodynamic analysis of the binary. Experiments at 1250 °C provide melt and a melting
341 loop that is still 0.2 X_{Mg} -units wide. Thermodynamic analysis of the pure siderite melting
342 curve from 6 to 20 GPa (Kang et al. 2015) permits calculating the metastable¹ melting curve
343 of siderite to 1264 °C at 3.5 GPa. This result is slightly above the temperature condition
344 where melt in the binary has been observed, suggesting a minimum. At 3.5 GPa, this

¹ with respect to magnetite+graphite+CO₂

345 minimum may lie within the uncertainties of the experiments and thermodynamic calculations,
346 nevertheless, at 10 GPa experiments have been run with two directly adjacent capsules: one
347 with pure siderite (pS-02, Kang et al. 2015) and one with a bulk $X_{Mg}=0.15$ (SM-02). In this
348 single experiment, with both capsules arranged symmetrically at the hotspot, the pure siderite
349 capsule remained unmolten, while the capsule with a bulk X_{Mg} of 0.15 showed 10-15% melt,
350 a clear indication of a minimum.

351 A non-ideal melting loop contrasts the diagram as drawn by Shatskiy et al. (2015a) who
352 show an ideal melting loop, based on a few experiments at relatively Fe-rich bulk
353 compositions ($X_{Mg}= 0.07-0.35$) at 1600-1700 °C at 6 GPa. In comparison to our work,
354 Shatskiy et al. (2015a) used natural siderite containing 6 mol% $MnCO_3$ and 7 mol% $MgCO_3$,
355 which may account for some difference in melting temperature. However, Shatskiy et al.
356 (2015a) propose stable melting of siderite at 6 GPa at a temperature slightly below 1600 °C
357 and observe complete melting of their $Fe_{0.87}Mn_{0.06}Mg_{0.07}CO_3$ composition at 1700 °C. This is
358 in wild contrast to the experimental data of Tao et al. (2013) and Kang et al. (2015), which
359 show siderite to be stable to 1400 °C but completely decomposed to magnetite+graphite+ CO_2
360 at 1450 °C, 6 GPa. Note that above 1450 °C magnetite+graphite+ CO_2 form a melt rich in
361 carbonate components. The data of Tao et al. (2013) and Kang et al. (2015) also indicate that
362 direct melting of siderite only occurs above 6 GPa (6.8 GPa in Kang et al. 2015). The
363 metastable pure siderite melting temperature at 6 GPa, as extrapolated from higher pressures,
364 is 1410 °C (Kang et al. 2015). This discrepancy was discussed by Shatskiy et al. (2015a)
365 aiming at experimental artefacts such as Fe-loss to the capsule but ignoring the autoredox-
366 decomposition of siderite. It remains unexplained why Tao et al. (2013) and Kang et al. (2015)
367 observe this redox decomposition while Shatskiy et al. (2015a) do not. Further, if the melting
368 temperature of pure siderite at 6 GPa would be almost 1600 °C instead of 1410 °C, as
369 suggested by Shatskiy et al. (2015a), then at 3.5 GPa the pure siderite melting temperature

370 would have to be considerably higher and the un-ideality and minimum of the system even
371 more pronounced.

372 At higher pressures of 10-20 GPa (Fig. 6) our experiments only constrain the behavior of
373 Fe-rich bulk compositions. Our melt model, which does not contain a pressure dependent non-
374 ideal term, indicates a flat minimum topology with melting temperatures from 1580 to
375 1840 °C, at X_{Mg} increasing from 0.2 to 0.28 with pressure. The calculated melting loop (based
376 solely on thermodynamic analysis of the experiments at 3.5 GPa) is in sufficient agreement
377 with the large scale melting (30-100%) observed in the experiments at 10-20 GPa, the small
378 melt fractions observed at lower temperatures being interpreted as hydrous melting caused by
379 moisture contamination of the starting material or H-gain through capsule wall diffusion (Fig.
380 6, diamonds).

381 *5.2 The pseudo-binary nature of FeCO_3 - MgCO_3*

382 Experiments in the Fe-Mg-C-O₂ system at 3.5 GPa show that siderite decomposition
383 through the auto-redox dissociation reaction (1) or decarbonation of the siderite-magnesite
384 solid solution (Sid-Mag_{ss}) according to reaction (2) interfere with the carbonate melting
385 reaction in the MgO-FeO-CO₂-system. For that reason, the simple binary FeCO_3 - MgCO_3 has
386 in reality the system components MgCO_3 - FeCO_3 -CO₂-Fe₂O₃, and is hence a pseudo-binary.
387 However, as long as the carbonate solid and melt are equilibrated, additional phases do not
388 influence this melting equilibrium and its thermodynamic analysis. The decomposition of the
389 siderite component hampers the determination of the melting loop:

390 (i) In the experiments, the formation of Fe-rich oxides through reaction (1) or (2)
391 shifts the bulk carbonate composition away from the siderite side towards MgCO_3
392 and experiments targeted at the melting loop often result in solid carbonate or melt
393 coexisting with oxides but not in the desired coexisting solid and liquid carbonate.

394 Obviously, when abundant low X_{Mg} iron oxides form (Table 1), the carbonate
395 phases alone do not mass balance the bulk composition anymore.

396 (ii) Secondly, further problems arise from the reaction products of reactions (1) and
397 (2): both reactions produce CO_2 ; this CO_2 was not observed as gas bubbles and is
398 likely to be dissolved in the carbonate melt.

399 (iii) Moreover, carbonate liquids do not exclusively quench to carbonates, but into a
400 mixture of carbonate and ferric iron containing oxides clearly visible in BSE
401 images (Fig. 2b, c, d, f) and sometimes identifiable as magnetite by Raman
402 spectroscopy. These textures are consistent with the results of Shatskiy et al.
403 (2015a, b; Figs. 2e, f, h and Fig. 1j, respectively), who observe a quench phase
404 from the liquid that is much brighter in BSE images than siderite.

405 To provide a first order assessment of the effect of non-stoichiometric melting, carbonate
406 phase equilibria were calculated in the system MgO-FeO-O-C including magnetite-
407 magnesioferrite and magnesiowustite solid solutions in addition to the carbonate models (Figs.
408 7-9). Graphite-saturated phase relations for this system are presented in 5 isothermal
409 triangular chemographic sections calculated for 1200 to 1675 °C at 3.5 GPa (Fig. 7). The
410 graphite-only saturation condition allows for three coexisting Fe-Mg-phases, as observed in
411 many experiments, in this case CO_2 -saturation cannot occur and the carbonate melt would be
412 the only liquid phase.

413 The same MgO-FeO join is projected from C and CO_2 such that f_{O_2} is constrained to the C-
414 CO-CO_2 (CCO) buffer into a T-X diagram (Fig. 8). These phase equilibria calculations
415 confirm the experimental observations (Fig. 4) that siderite-rich carbonate phases become
416 unstable at 3.5 GPa and will always transform into ferric components forming Mt_{ss} below
417 ~1500 °C at the Fe side of this pseudo-binary. Above ~1500 °C the computation predicts
418 stability fields for magnesiowustite coexisting with the carbonate liquid field towards the Mg
419 side along the FeO-MgO join projected through O_2 and C, as it is depicted in the

420 chemographic triangles in Fig. 7. In the experiments we used inner graphite capsules, but fluid
421 vapor bubbles of CO₂ were not observed at 3.5 GPa, hence, the experimental f_{O2} may well be
422 below CCO.

423 A calculation at 1400 °C, 3.5 GPa in log(f_{O2}) vs. X_{Mg} space, expanded around CCO,
424 suggests that small variations in f_{O2} below CCO would have a large effect on the
425 magnesiowustite composition and on liquid compositions (Fig. 9), but would cause little or
426 marginal differences in the Mt_{ss} stability. The computed phase diagram also shows that below
427 an f_{O2} of CCO-0.4 the stability range of Fe-Mg carbonates decreases distinctively towards the
428 Mg side along the FeO-MgO join. The carbonate melt compositions are not located on the
429 same binary of the solid carbonates, analogous to the diopside-anorthite-albite system, where
430 liquids are expected to be on a cotectic; see Fig. 10.25 in Philpotts (1990). Our two
431 component thermodynamic melt model includes hence a deviation of the melt composition
432 from the simple binary, a situation not much different from many solid solutions, where pure
433 ferrous endmembers do not exist but always contain some ferric iron (e.g. biotite, staurolite,
434 saphirine, talc).

435

436 **6. Concluding remarks**

437 In this study we present experiments on the FeCO₃-MgCO₃ join at 3.5-20 GPa, which
438 allow depicting the melting loop in T-X diagrams. The melting loop is asymmetrical and has a
439 thermal minimum at Fe-rich bulk compositions. A regular solution model is adequate to
440 represent these phase relations over the pressure-temperature range of our observations.
441 Interpretation of the system at Fe-rich compositions is complicated by problems of Fe²⁺-
442 oxidation and excess CO₂ dissolved in the melt. For the melting of basaltic and peridotitic
443 bulk compositions a liquid Fe-carbonate endmember is needed to calculate phase relations,
444 although the dominant carbonate melt components are the Mg and Ca ones. For carbonated

445 pelites, partial carbonate melts may reach down to $X_{\text{Mg}} = 0.24$ (Grassi and Schmidt 2011), at
446 the extreme banded iron formations may produce almost pure siderite melts.

447

448 **Acknowledgements**

449 Thanks to L. Ramalingam for conducting some of the siderite-magnesite experiments at 3.5
450 GPa. We are thankful to C. Liebske for discussion and technical support in the laboratory, and
451 to T. Good and B. Zürcher for mechanical support. We also thank X. Zhong and D. Miron for
452 discussions about thermodynamic solution models. This study was made possible through
453 grant SNF-200020-130100/1 and 200020-140541/1.

454

455 **Figure captions**

456 **Fig.1** Schreinemaker analysis of the melting relations of siderite and magnesite at their
457 lowest melting pressures. The MgO-CO₂ system (a) behaves as a true binary and has a simple
458 topology, but phase relations describing siderite melting require 3 system components (FeO-
459 C-O₂), opening up a magnetite+graphite field (b). Wustite only becomes stable at higher
460 temperatures than siderite stability, a consequence of the discordance between the CCO buffer
461 and the Fe-O buffers (see insert). The topology of the FO-C-CO₂ system is drawn for two
462 options: in black and blue reactions for a siderite melt with stoichiometric siderite
463 composition, in black and red for siderite melt with a minor ferric component and dissolved
464 CO₂. Approximate pressures and/or temperatures are indicated, for magnesite as determined
465 by Irvine and Wyllie (1975), for siderite as determined by Tao et al. (2013) and Kang et al.
466 (2015). Phase abbreviations in text, figures and tables are: Wu = wustite; Carb_{ss} = siderite-
467 magnesite solid solution; Mt_{ss} = magnetite-magnesioferrite solid solution; Gph = graphite; Liq
468 = carbonate melt (containing Fe-oxide quench phases); Mw_{ss} = wustite-periclase solid
469 solution; Mag_{rem} = magnesite remnant stemming from starting material; Carb-q = carbonate

470 quench; Mt-q = magnetite quench; MgCO₃L = magnesite liquid; FeCO₃L = siderite liquid;
471 Sid = siderite; Mag = magnesite; Mt = magnetite; Per = periclase;

472

473

474 **Fig. 2** Back-scattered electron (BSE) images of typical run products at 3.5 GPa showing
475 subsolidus, near-solidus and supersolidus conditions. **(a)** Carbonates at subsolidus conditions
476 with substantial decomposition to magnetite solid solution. Note that the bulk X_{Mg} is 0.1 but
477 the resulting carbonate has $X_{Mg}=0.61$. **(b)** Partial melting of carbonates to dendritic carbonate
478 melt consisting of carbonate quench and iron oxide fractions. Some melt infiltrates the
479 innermost part of the graphite capsule (bottom of image). **(c)** Stable Fe-Mg-carbonates
480 coexisting with carbonate melt and some wustite. **(d)** Carbonate melt coexisting with crystal
481 carbonates; quenched carbonate melts are interstitial to the rounded carbonate grains. **(e)** At
482 subsolidus conditions discrete carbonates appear with minor Mt_{ss} at low run times. **(f)**
483 Supersolidus condition, carbonates are completely molten with an intergrowth of carbonate
484 and magnetite quench.

485 **Fig. 3** BSE images of run products at 10-20 GPa. **(a)** Monomineralic stable siderite
486 assemblage in gold-palladium capsule at 10 GPa, 1500 °C from Kang et al. (2015). **(b)** Low
487 degree of partial melting of Mg-bearing siderite with the starting composition Mg_{0.15}Fe_{0.85}CO₃
488 at 10 GPa, 1500 °C. A similar amount of melt persists over a temperature range of 30-200 °C
489 and is interpreted as melting caused by small amounts of H₂O present in the capsule (see text).
490 **(c)** Coexistence of siderite-magnesite solid solution with Fe-Mg carbonate melt at 13.6 GPa,
491 1700 °C. **(d)** Melting of Fe-Mg carbonates at 20 GPa, 1860 °C. Abbreviations as in Fig. 1

492

493 **Fig. 4** Triangular isothermal sections of the most critical experimental runs showing
494 compositions of run products in the FeO-MgO-O₂ system projected through graphite from
495 1575 to 1200 °C at 3.5 GPa. Note that melt compositions in e) and f) exhibit large standard

496 deviations (see also Fig. 5 and Table 1). Coexisting phases within each experiment were
497 connected by solid tie-lines. Symbol or tie-line labels indicate experiment number, see also
498 Table 1. Abbreviations as in Fig. 1

499

500 **Fig. 5** Isobaric T - X diagram in the simple FeCO_3 - MgCO_3 binary at 3.5 GPa, depicting
501 experimental data of stable carbonate solid and liquid pairs with the calculated melting loop
502 employed by Perple_X 6.6.9 (Connolly 2009). The pure siderite melting temperature is
503 calculated from Kang et al. (2015), note that this melting temperature is metastable. The pure
504 magnesite melting temperature is after Irving and Wyllie (1975) and calculated for the pure
505 magnesite melting curve. Standard thermodynamic properties for the end-members siderite
506 and FeCO_3L are adopted from Kang et al. (2015). Thermodynamic data for magnesite and
507 MgCO_3L are from Merlini et al. (2016) and this study. We used our melt solution model
508 termed LIQ(NK) combined with the solid solution model for ternary Ca-Mg-Fe carbonates
509 termed dis(EF) from Franzolin et al. (2010). Dashed lines represent tie lines between
510 coexisting solid and liquid pairs. Thin solid lines display error bars in terms of standard
511 deviation. The symbols and error bars of experiments at 1250 °C are not superimposed for
512 clarity. Note that the Fe-rich side at $X_{\text{Mg}} < 0.25$ is metastable with respect to magnetite+
513 CO_2 +graphite. The position of the minimum is calculated from the fit of the loop to the
514 experimental data (see text). Abbreviations as in Fig. 1

515

516 **Fig. 6** Isobaric T - X sections of the Fe-rich side of the FeCO_3 - MgCO_3 join at 10, 13.6 and
517 20 GPa. Experimental compositions of coexisting carbonate solid (filled symbols) and liquid
518 (open symbols) pairs are from this study, pure siderite experiments are from Kang et al.
519 (2015). Half-filled symbols illustrate partial melting. Blue diamonds indicate experiments
520 with <15% melt, interpreted as melting in the presence of minor H_2O unavoidable in this kind
521 of starting material. The melting loops including a minimum were calculated employing

522 Perple_X 6.6.9 (Connolly 2009). Note that the liquid solution model is entirely based on data
523 at 3.5 GPa. The small deviation between the calculated loop and the experimental data at high
524 pressure does not warrant an unideal pressure-term in the liquid solution model. The
525 thermodynamic data of all end-members are the same as in Fig. 5. Horizontal solid lines are
526 error bars in terms of standard deviation. Abbreviations as in Fig. 1

527
528 **Fig. 7** Calculated chemographic diagrams in the FeO-MgO-O₂ ternary saturated in graphite,
529 showing stable phase assemblages in isothermal sections from 1200 to 1675 °C employing
530 Perple_X 6.6.9 (Connolly 2009). For these calculations we included the ideal solid solution
531 models for magnetite-magnesioferrite (MF) and for periclase-wustite (P) from Perple_X in
532 addition to the carbonate models. Initial melting appears between 1200 and 1300 °C, see text.
533 White triangles suggest 3-phase fields where the phases at their corner points are stable with
534 each other. Grey fields represent two-phase fields between opposing mineral assemblages.
535 Solid solutions are indicated by bold lines. Abbreviations as in Fig. 1

536
537 **Fig. 8** Calculated isobaric *T-X* diagram along the FeO-MgO join projected through CCO,
538 i.e. saturated in CO₂ fluid and graphite at 3.5 GPa employing Perple_X 6.6.9 (Connolly 2009).
539 The solution models used in this computation are the same as in Fig. 6. CO₂ is chosen as the
540 independent saturated fluid component and O₂ as the saturated or buffered component. The
541 fluid EoS is X(O) GCOH-fluid hybrid-EoS from Connolly and Cesare (1993). Carbonates are
542 unstable near the siderite side where magnetite-magnesioferrite solid solution forms.
543 Thermodynamic properties of wustite, periclase, magnetite and magnesioferrite are from
544 Holland and Powell (2011). The thermodynamic data set of Fe-Mg carbonates and their melts
545 are the same as described in Fig. 4. Abbreviations as in Fig. 1

546

547 **Fig. 9** Calculated phase relations in $\log(f_{O_2})$ vs. $X_{Mg}=Mg/(Fe_{tot}+Mg)$ expanded around the
548 CCO buffer at 1400 °C, 3.5 GPa portraying that small variations in f_{O_2} have large effects on
549 magnesiowustite and on carbonate liquid compositions. As the experiments are most probably
550 below CCO the phase equilibria computation is in good agreement with the experimental
551 observations of $Mw_{u_{ss}}$ compositions deviating to higher X_{Mg} due to the change of f_{O_2} . This
552 effect is prominently important, since carbonates become unstable to very low f_{O_2} towards the
553 Mg side of this pseudo-binary. Note that the stability boundaries of the carbonate liquid and
554 solid field would slightly extended at higher f_{O_2} due to the ferric iron component in the melt.
555 The solution models used are the same as in Figs. 7 & 8.

556

557 **Appendix**

558 Thermodynamic modeling is used to determine the general shape of the stability fields and the
559 relations between the different phases occurring in the system. Furthermore, it allows
560 subsequent comparison between calculated and experimentally determined stability data. In
561 Earth sciences, thermodynamic melt models have been offered for granitic (Holland and
562 Powell 2001, Gualda et al. 2012) and basaltic silicate melts (Ghiorso and Sack 1995). In the
563 following section, we use our experimental data to develop a thermodynamic model for
564 carbonate melts within the $FeCO_3$ - $MgCO_3$ system valid to 20 GPa.

565 The thermodynamic properties of the two liquid endmembers $FeCO_3L$ and $MgCO_3L$
566 constitute the basis of the solution model of carbonate liquids along the $FeCO_3$ - $MgCO_3$ join.
567 The Gibbs energy of such a solution phase contains two terms in addition to the pure
568 mechanical mixing:

$$569 \quad G_{sol} = G^{mech} + G^{conf} + G^{ex}$$

570 The molar Gibbs energy of a solution G_{sol} may hence be further formulated as

$$G_{sol} = \sum_{i=1}^n X_i G_i^0 + RT \sum_{i=1}^n X_i \ln X_i + RT \sum_{i=1}^n X_i \ln \gamma_i .$$

571 The first term is the energy arising from mechanically mixing of the endmembers and the
 572 second term corresponds to the configurational entropy. The third term accounts for unideal
 573 energetic effects caused by distortions of the atomic structure (e.g., strain) through mixing and
 574 is the (excess) Gibbs energy of mixing G^{ex} .

575 At equilibrium, the chemical potentials of the components in the system (or their partial molar
 576 Gibbs energies) are required to be equal in coexisting phases, i.e. in the melt and crystal. If μ
 577 is the partial molar Gibbs energy, the following equations are valid for coexisting carbonate
 578 crystals and melts:

$$579 \quad \mu_{Sid}^S = \mu_{Sid}^L$$

$$580 \quad \mu_{Mag}^S = \mu_{Mag}^L$$

581 where S and L are the solid and liquid phases; Sid = siderite and Mag = magnesite.

582 The excess term of the solid phase is modeled with the Van Laar parameters α and one
 583 interaction parameter W (in J/mol) based on the work of Franzolin et al. (2010). The activity
 584 coefficient term $RT \ln \gamma_i$ of the solid phase is defined as

$$585 \quad RT \ln \gamma_i = \frac{2\alpha_i}{\alpha_i + \alpha_j} \varphi_j^2 W_{ij}$$

586 (Holland and Powell 2003) where

$$587 \quad \varphi_i = \frac{p_i \alpha_i}{\sum_{j=1}^n p_j \alpha_j} .$$

588 The proportion p is equal to the mole fraction since there are no order-disorder phenomena in
 589 this system.

590 The excess term of the melt phase was modeled according to the symmetrical regular
 591 (Hildebrand 1929) and macroscopic (asymmetrical) subregular formalism (Hardy 1953) with
 592 one (W) or two (W_{12} , W_{21}) different Margules interaction parameters. The latter describe the
 593 asymmetric activity-composition relationship in Fe-Mg-carbonate melts.

594 For a n component system, the excess Gibbs energy of an asymmetric, subregular solution
 595 can be written in general terms as

$$596 \quad G^{ex} = \sum_i^n \sum_{<j}^n X_i X_j (X_j w_{ij} + X_i w_{ji})$$

597 The activity coefficients of the two end-members in a subregular solution are given as

$$598 \quad RT \ln \gamma_{sid} = (1 - X_{sid}) X_{mag} [w_{sm} + 2(w_{ms} - w_{sm}) X_{sid}]$$

$$599 \quad RT \ln \gamma_{mag} = X_{sid} (1 - X_{mag}) [w_{ms} + 2(w_{sm} - w_{ms}) X_{mag}]$$

600 For $w_{12}=w_{21}$, these equations reduce to the expressions for a regular solution, i.e. the
 601 interaction parameters are composition independent. For a regular binary solution with the
 602 endmembers 1 and 2, G^{ex} is given by

$$603 \quad G^{ex} = X_1 X_2 w_{12}$$

604 where $X_1 + X_2 = 1$ and only one of the two composition variables is independent. After
 605 choosing X_2 as the independent variable i.e. $X \equiv X_2$, the activity terms can be expressed as

$$606 \quad RT \ln \gamma_{sid} = X^2 w_{sm}$$

$$607 \quad RT \ln \gamma_{mag} = (1 - X)^2 w_{sm}.$$

608 We tested both models for the excess term of the liquid by solving equations 11 and 12 at
 609 each experimental data point. Comparison of the results yielded similar interaction parameters
 610 and no significant improvement of the fit for the subregular model. We hence use the regular
 611 model with only one parameter.

612 The interaction parameters w_{ij} can be further decomposed into enthalpic (w_{ij}^H), entropic (w_{ij}^S)
613 and volumetric terms (w_{ij}^V) according to

$$614 \quad w = w^H + w^S T + w^V P .$$

615 Introducing a temperature dependence to the interaction parameter w_S has not led to a better fit
616 of the experiments, but to an unreasonable extrapolation in temperature producing new phase
617 fields at high temperatures. So far, a pressure dependence of the interaction parameter,
618 applicable up to 20 GPa, is not needed since the location of the minimum with pressure fits
619 sufficiently with the (interpreted) melting temperatures on the Fe-rich side of the binary.
620 Nevertheless, we calculated the enthalpic terms w_{Sid}^H and w_{Mag}^H from the experimentally
621 determined phase diagram at 3.5 GPa and average them to $W_{MgFe} = W_{FeMg} = -7600$ J/mol (Table
622 2). The resultant energetic parameter is negative, maintaining a convex downward melting
623 loop with a minimum near the siderite side.

624

625

626 **References**

- 627 Beukes, N.J. & J. Gutzmer (2008) Origin and Paleoenvironmental Significance of Major Iron
628 Formations at the Archean-Paleoproterozoic Boundary. Banded Iron Formation-
629 Related High-Grade Iron Ore, 15, 5-47.
- 630 Biellmann, C., P. Gillet, F. Guyot, J. Peyronneau & B. Reynard (1993) Experimental-
631 Evidence for Carbonate Stability in the Earth's Lower Mantle. Earth and Planetary
632 Science Letters, 118, 31-41.
- 633 Boulard, E., N. Menguy, A.L. Auzende, K. Benzerara, H. Bureau, D. Antonangeli, A. Corgne,
634 G. Morard, J. Siebert, J.P. Perrillat, F. Guyot & G. Fiquet (2012) Experimental
635 investigation of the stability of Fe-rich carbonates in the lower mantle. Journal of
636 Geophysical Research-Solid Earth, 117.

637 Brey, G.P., V.K. Bulatov & A.V. Gurnis (2009) Influence of water and fluorine on melting of
638 carbonated peridotite at 6 and 10 GPa. *Lithos*, 112, 249-259.

639 Brey, G.P., V.K. Bulatov, A.V. Gurnis & Y. Lahaye (2008) Experimental melting of
640 carbonated peridotite at 6-10 GPa. *Journal of Petrology*, 49, 797-821.

641 Buckley, H.A. & A.R. Woolley (1990) Carbonates of the Magnesite Siderite Series from 4
642 Carbonatite Complexes. *Mineralogical Magazine*, 54, 413-418.

643 Connolly, J.A.D. (2009) The geodynamic equation of state: What and how. *Geochemistry
644 Geophysics Geosystems*, 10.

645 Connolly, J.A.D. & B. Cesare (1993) C-O-H-S Fluid Composition and Oxygen Fugacity in
646 Graphitic Metapelites. *Journal of Metamorphic Geology*, 11, 379-388.

647 Dasgupta, R. & M.M. Hirschmann (2006) Melting in the Earth's deep upper mantle caused by
648 carbon dioxide. *Nature*, 440, 659-662.

649 --- (2010) The deep carbon cycle and melting in Earth's interior. *Earth and Planetary Science
650 Letters*, 298, 1-13.

651 Dasgupta, R., M.M. Hirschmann & N. Dellas (2005) The effect of bulk composition on the
652 solidus of carbonated eclogite from partial melting experiments at 3 GPa.
653 *Contributions to Mineralogy and Petrology*, 149, 288-305.

654 Dasgupta, R., M.M. Hirschmann & A.C. Withers (2004) Deep global cycling of carbon
655 constrained by the solidus of anhydrous, carbonated eclogite under upper mantle
656 conditions. *Earth and Planetary Science Letters*, 227, 73-85.

657 Davidson, P.M. (1994) Ternary Iron, Magnesium, Calcium Carbonates - a Thermodynamic
658 Model for Dolomite as an Ordered Derivative of Calcite-Structure Solutions.
659 *American Mineralogist*, 79, 332-339.

660 Dobson, D.P. & J.P. Brodholt (2005) Subducted banded iron formations as a source of
661 ultralow-velocity zones at the core-mantle boundary. *Nature*, 434, 371-374.

662 Eiler, J.M., J.W. Valley, C.M. Graham & J. Fournelle (2002) Two populations of carbonate in
663 ALH84001: Geochemical evidence for discrimination and genesis. *Geochimica Et
664 Cosmochimica Acta*, 66, 1285-1303.

665 Falloon, T.J. & D.H. Green (1989) The Solidus of Carbonated, Fertile Peridotite. *Earth and
666 Planetary Science Letters*, 94, 364-370.

667 Fiquet, G., F. Guyot, M. Kunz, J. Matas, D. Andrault & M. Hanfland (2002) Structural
668 refinements of magnesite at very high pressure. *American Mineralogist*, 87, 1261-
669 1265.

670 Franzolin, E., M.W. Schmidt & S. Poli (2011) Ternary Ca-Fe-Mg carbonates: subsolidus
671 phase relations at 3.5 GPa and a thermodynamic solid solution model including
672 order/disorder. *Contributions to Mineralogy and Petrology*, 161, 213-227.

673 French, B.M. (1971) Stability Relations of Siderite (FeCO_3) in System Fe-C-O. *American*
674 *Journal of Science*, 271, 37-78.

675 Ghiorso, M.S. & R.O. Sack (1995) Chemical Mass-Transfer in Magmatic Processes .4. A
676 Revised and Internally Consistent Thermodynamic Model for the Interpolation and
677 Extrapolation of Liquid-Solid Equilibria in Magmatic Systems at Elevated-
678 Temperatures and Pressures. *Contributions to Mineralogy and Petrology*, 119, 197-
679 212.

680 Ghosh, S., E. Ohtani, K.D. Litasov & H. Terasaki (2009) Solidus of carbonated peridotite
681 from 10 to 20 GPa and origin of magnesiocarbonatite melt in the Earth's deep mantle.
682 *Chemical Geology*, 262, 17-28.

683 Goldsmith, J.R., D.L. Graf, J. Witters & D.A. Northrop (1962) Studies in the System CaCO_3 -
684 MgCO_3 - FeCO_3 .1. Phase Relations. 2. A Method for Major-Element Spectrochemical
685 Analysis. 3. Compositions of Some Ferroan Dolomites. *Journal of Geology*, 70, 659-
686 688.

687 Grassi, D. & M.W. Schmidt (2011) Melting of carbonated pelites at 8-13 GPa: generating K-
688 rich carbonatites for mantle metasomatism. *Contributions to Mineralogy and*
689 *Petrology*, 162, 169-191.

690 Gualda, G.A.R., M.S. Ghiorso, R.V. Lemons & T.L. Carley (2012) Rhyolite-MELTS: a
691 Modified Calibration of MELTS Optimized for Silica-rich, Fluid-bearing Magmatic
692 Systems. *Journal of Petrology*, 53, 875-890.

693 Hardy, H.K. (1953) A Sub-Regular Solution Model and Its Application to Some Binary Alloy
694 Systems. *Acta Metallurgica*, 1, 202-209.

695 Hildebrand, J.H. (1929) Solubility XII Regular solutions. *Journal of the American Chemical*
696 *Society*, 51, 66-80.

697 Holland, T.J.B. & R. Powell (1998) An internally consistent thermodynamic data set for
698 phases of petrological interest. *Journal of Metamorphic Geology*, 16, 309-343.

699 --- (2001) Calculation of phase relations involving haplogranitic melts using an internally
700 consistent thermodynamic dataset. *Journal of Petrology*, 42, 673-683.

701 --- (2003) Activity-composition relations for phases in petrological calculations: an
702 asymmetric multicomponent formulation. *Contributions to Mineralogy and Petrology*,
703 145, 492-501.

704 --- (2011) An improved and extended internally consistent thermodynamic dataset for phases
705 of petrological interest, involving a new equation of state for solids. *Journal of*
706 *Metamorphic Geology*, 29, 333-383.

707 Irving, A.J. & P.J. Wyllie (1975) Subsolidus and Melting Relationships for Calcite, Magnesite
708 and Join CaCO_3 - MgCO_3 to 36 Kb. *Geochimica Et Cosmochimica Acta*, 39, 35-53.

709 Isshiki, M., T. Irifune, K. Hirose, S. Ono, Y. Ohishi, T. Watanuki, E. Nishibori, M. Takata &
710 M. Sakata (2004) Stability of magnesite and its high-pressure form in the lowermost
711 mantle. *Nature*, 427, 60-63.

712 Kang, N., M.W. Schmidt, S. Poli, E. Franzolin & J.A.D. Connolly (2015) Melting of siderite
713 to 20 GPa and thermodynamic properties of FeCO_3 -melt. *Chemical Geology*, 400, 34-
714 43.

715 Katsura, T. & E. Ito (1990) Melting and Subsolidus Phase-Relations in the MgSiO_3 - MgCO_3
716 System at High-Pressures - Implications to Evolution of the Earth's Atmosphere. *Earth*
717 *and Planetary Science Letters*, 99, 110-117.

718 Keppeler, H., M. Wiedenbeck & S.S. Shcheka (2003) Carbon solubility in olivine and the
719 mode of carbon storage in the Earth's mantle. *Nature*, 424, 414-416.

720 Kerrick, D.M. & J.A.D. Connolly (2001) Metamorphic devolatilization of subducted marine
721 sediments and the transport of volatiles into the Earth's mantle. *Nature*, 411, 293-296.

722 --- (2001b) Metamorphic devolatilization of subducted oceanic metabasalts: implications for
723 seismicity, arc magmatism and volatile recycling. *Earth and Planetary Science Letters*,
724 189, 19-29.

725 Kholodov, V.N. & G.Y. Butuzova (2008) Siderite formation and evolution of sedimentary
726 iron ore deposition in the Earth's history. *Geology of Ore Deposits*, 50, 299-319.

727 Klein-BenDavid, O., A.M. Logvinova, M. Schrauder, Z.V. Spetius, Y. Weiss, E.H. Hauri, F.V.
728 Kaminsky, N.V. Sobolev & O. Navon (2009) High-Mg carbonatitic microinclusions in
729 some Yakutian diamonds-a new type of diamond-forming fluid. *Lithos*, 112, 648-659.

730 Klein, C. (2005) Some Precambrian banded iron-formations (BIFs) from around the world:
731 Their age, geologic setting, mineralogy, metamorphism, geochemistry, and origin.
732 *American Mineralogist*, 90, 1473-1499.

733 Koziol, A.M. (2004) Experimental determination of siderite stability and application to
734 Martian Meteorite ALH84001. *American Mineralogist*, 89, 294-300.

735 Litasov, K.D., Y.W. Fei, E. Ohtani, T. Kuribayashi & K. Funakoshi (2008) Thermal equation
736 of state of magnesite to 32 GPa and 2073 K. *Physics of the Earth and Planetary*
737 *Interiors*, 168, 191-203.

738 Litasov, K.D., A. Shatskiy, P.N. Gavryushkin, I.S. Sharygin, P.I. Dorogokupets, A.M.
739 Dymshits, E. Ohtani, Y. Higo & K. Funakoshi (2013) P-V-T equation of state of
740 siderite to 33 GPa and 1673 K. *Physics of the Earth and Planetary Interiors*, 224, 83-
741 87.

742 Mann, U. & M.W. Schmidt (2015) Melting of pelitic sediments at subarc depths: 1. Flux vs.
743 fluid-absent melting and a parameterization of melt productivity. *Chemical Geology*,
744 404, 150-167.

745 Merlini, M., S. Tumiatì, P. Lotti, F. Sapelli, P. Fumagalli, D. Gatta, M. Abdellatif, J. Plaisier,
746 A. Lausi, M. Hanfland, W. Crichton, J. Chantel, J. Guignard, A. Pavese & S. Poli
747 (2016) High-temperature and high-pressure behavior of carbonates in the ternary
748 diagram $\text{CaCO}_3\text{-MgCO}_3\text{-FeCO}_3$. *American Mineralogist*, 101, 1423-1430.

749 Molina, J.F. & S. Poli (2000) Carbonate stability and fluid composition in subducted oceanic
750 crust: an experimental study on $\text{H}_2\text{O-CO}_2$ -bearing basalts. *Earth and Planetary
751 Science Letters*, 176, 295-310.

752 Morris, R.V., S.W. Ruff, R. Gellert, D.W. Ming, R.E. Arvidson, B.C. Clark, D.C. Golden, K.
753 Siebach, G. Klingelhofer, C. Schroder, I. Fleischer, A.S. Yen & S.W. Squyres (2010)
754 Identification of Carbonate-Rich Outcrops on Mars by the Spirit Rover. *Science*, 329,
755 421-424.

756 Panero, W.R. & J.E. Kabbes (2008) Mantle-wide sequestration of carbon in silicates and the
757 structure of magnesite II. *Geophysical Research Letters*, 35.

758 Philipp, R.W. (1998) Phasenbeziehungen im System $\text{MgO-H}_2\text{O-CO}_2\text{-NaCl}$. Dissertation. ETH
759 Zurich.

760 Philpotts, A.R. (1990) Principles of igneous and metamorphic petrology Anthony R. Philpotts.
761 Prentice Hall, Englewood Cliffs, 498 p.

762 Polat, A., A.W. Hofmann & M.T. Rosing (2002) Boninite-like volcanic rocks in the 3.7-3.8
763 Ga Isua greenstone belt, West Greenland: geochemical evidence for intra-oceanic
764 subduction zone processes in the early Earth. *Chemical Geology*, 184, 231-254.

765 Poli, S., E. Franzolin, P. Fumagalli & A. Crottini (2009) The transport of carbon and
766 hydrogen in subducted oceanic crust: An experimental study to 5 GPa. *Earth and
767 Planetary Science Letters*, 278, 350-360.

768 Rosenberg, P.E. (1967) Subsolvus Relations in System $\text{CaCO}_3\text{-MgCO}_3\text{-FeCO}_3$ between 350
769 Degrees and 550 Degrees C. *American Mineralogist*, 52, 787-796.

770 Shatskiy, A., K.D. Litasov, E. Ohtani, Y.M. Borzdov, A.I. Khmel'nikov & Y.N. Palyanov
771 (2015a) Phase relations in the K_2CO_3 - $FeCO_3$ and $MgCO_3$ - $FeCO_3$ systems at 6 GPa
772 and 900-1700 °C. *Eur. J. Mineral.*, 27 (4), 487-499.

773 Shatskiy, A., S.V. Rashchenko, E. Ohtani, K.D. Litasov, M.V. Khlestov, Y.M. Borzdov, I.N.
774 Kupriyanov, I.S. Sharygin & Y.N. Palyanov (2015b) The system Na_2CO_3 - $FeCO_3$ at 6
775 GPa and its relation to the system Na_2CO_3 - $FeCO_3$ - $MgCO_3$. *American Mineralogist*,
776 100, 130-137.

777 Shcheka, S.S., M. Wiedenbeck, D.J. Frost & H. Keppler (2006) Carbon solubility in mantle
778 minerals. *Earth and Planetary Science Letters*, 245, 730-742.

779 Stachel, T., J.W. Harris, G.P. Brey & W. Joswig (2000) Kankan diamonds (Guinea) II: lower
780 mantle inclusion parageneses. *Contributions to Mineralogy and Petrology*, 140, 16-27.

781 Stewart, A.J., W. van Westrenen, M.W. Schmidt & E. Melekhova (2006) Effect of gasketing
782 and assembly design: a novel 10/3.5mm multi-anvil assembly reaching perovskite
783 pressures. *High Pressure Research*, 26, 293-299.

784 Tao, R.B., Y.W. Fei & L.F. Zhang (2013) Experimental determination of siderite stability at
785 high pressure. *American Mineralogist*, 98, 1565-1572.

786 Thomsen, T.B. & M.W. Schmidt (2008) Melting of carbonated pelites at 2.5-5.0 GPa, silicate-
787 carbonatite liquid immiscibility, and potassium-carbon metasomatism of the mantle.
788 *Earth and Planetary Science Letters*, 267, 17-31.

789 Wallace, M.E. & D.H. Green (1988) An Experimental-Determination of Primary Carbonatite
790 Magma Composition. *Nature*, 335, 343-346.

791 Wang, A., J.D. Pasteris, H.O.A. Meyer & M.L. DeleDuboi (1996) Magnesite-bearing
792 inclusion assemblage in natural diamond. *Earth and Planetary Science Letters*, 141,
793 293-306.

794 Weidner, J.R. (1972) Equilibria in System Fe-C-O. 1. Siderite-Magnetite-Carbon-Vapor
795 Equilibrium from 500 to 10,000 Bars. *American Journal of Science*, 272, 735-751.

796 Yaxley, G.M. & G.P. Brey (2004) Phase relations of carbonate-bearing eclogite assemblages
797 from 2.5 to 5.5 GPa: implications for petrogenesis of carbonatites. *Contributions to*
798 *Mineralogy and Petrology*, 146, 606-619.

799 Yaxley, G.M. & D.H. Green (1994) Experimental Demonstration of Refractory Carbonate-
800 Bearing Eclogite and Siliceous Melt in the Subduction Regime. *Earth and Planetary*
801 *Science Letters*, 128, 313-325.

802

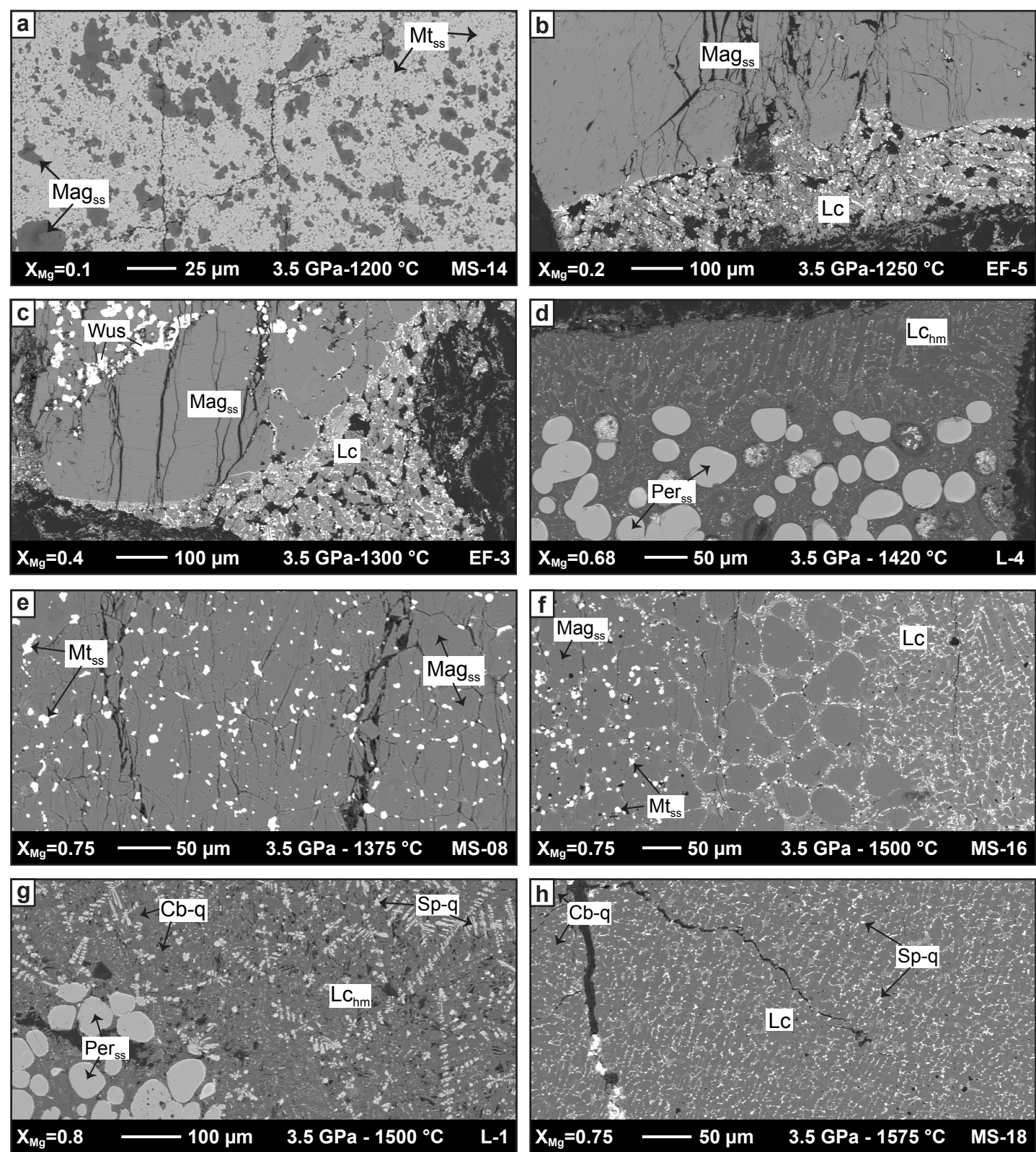


Fig. 1
1.5 or 2 column

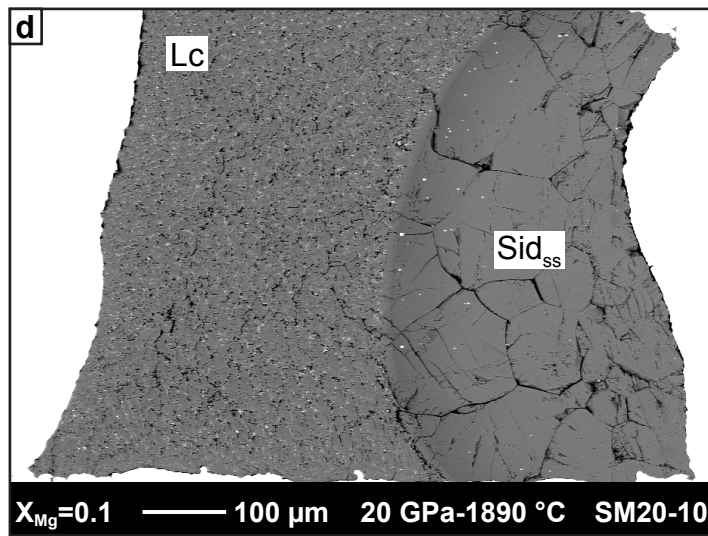
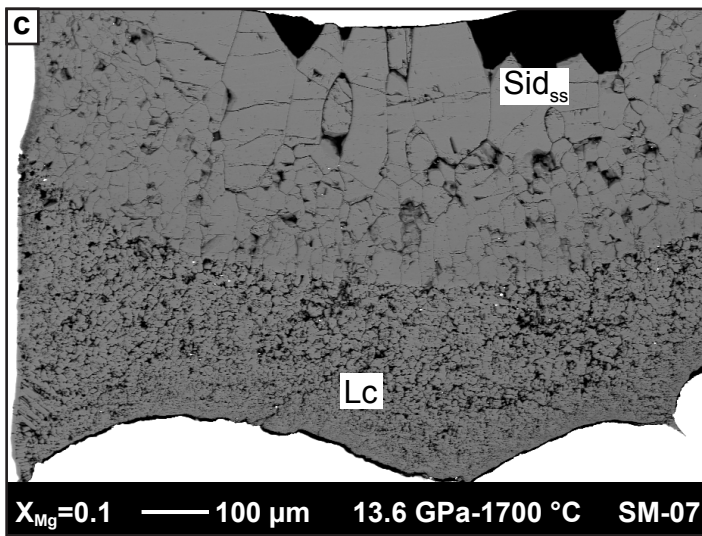
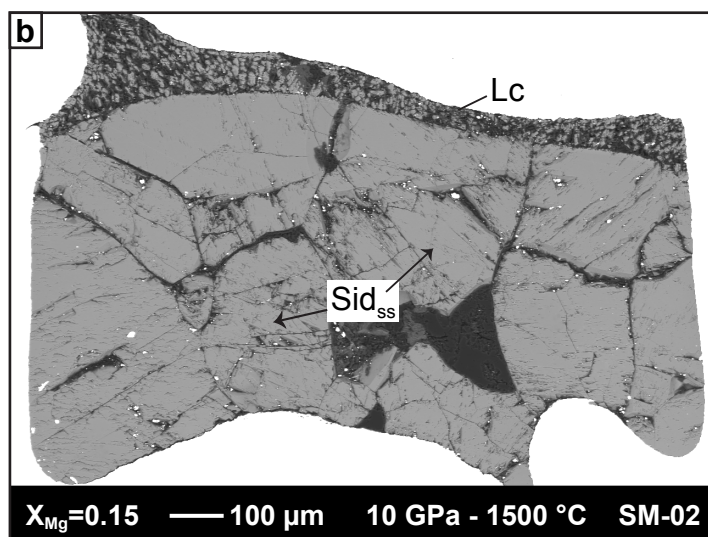
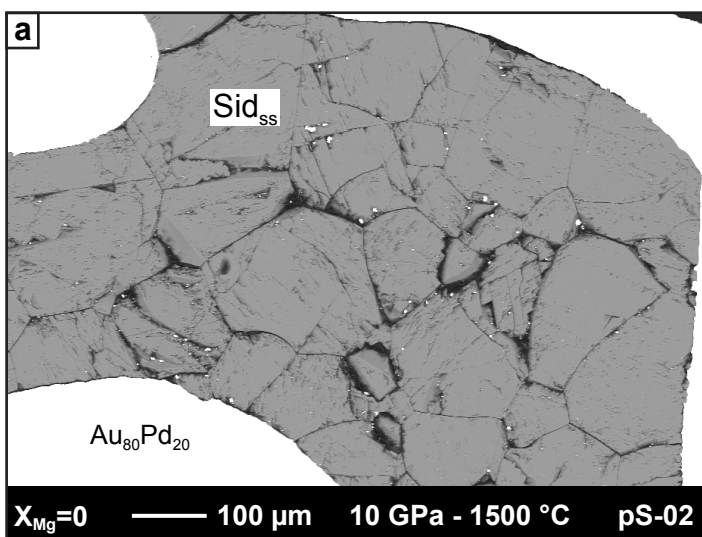


Fig. 2
1.5 or 2 column

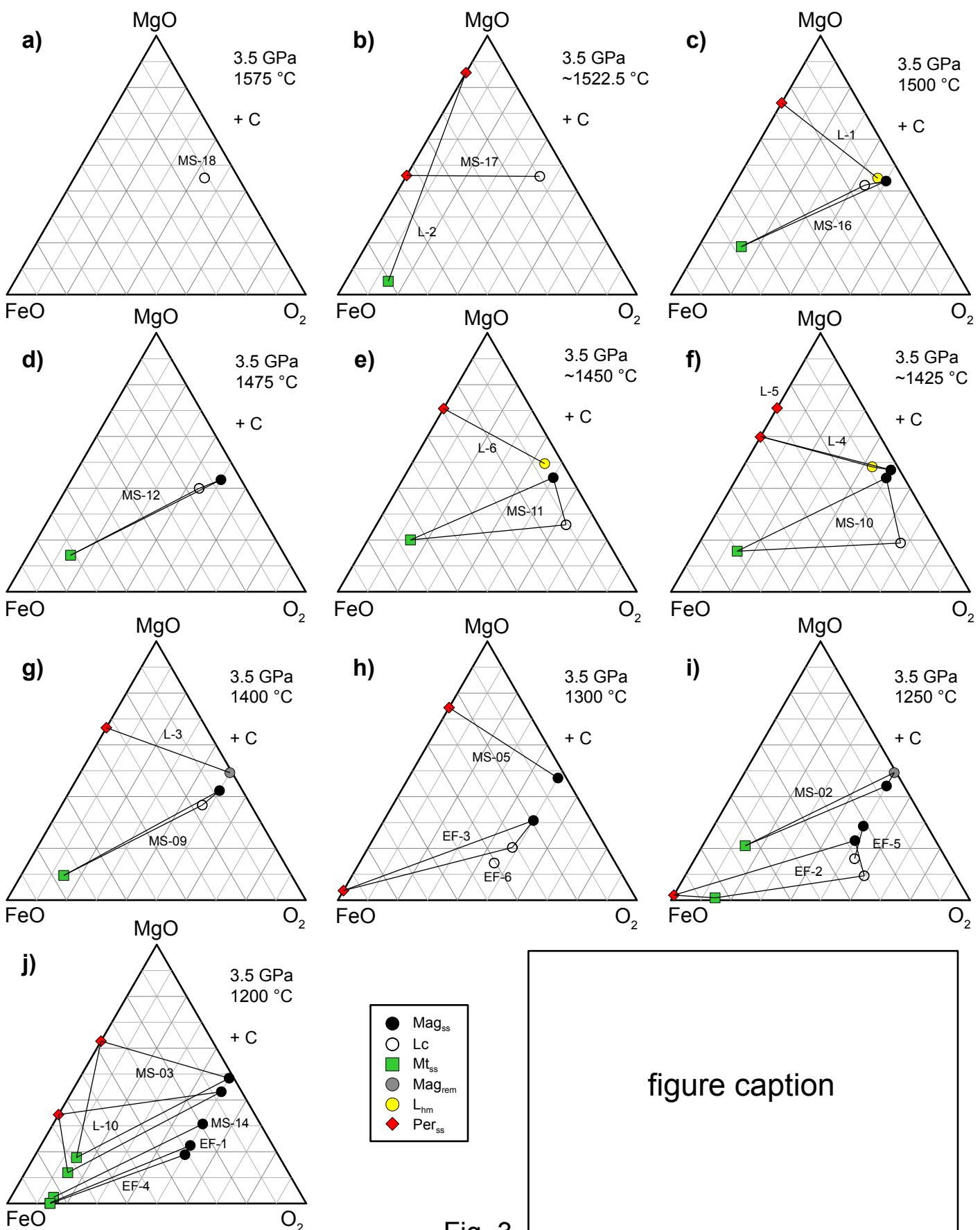


figure caption

Fig. 3

1.5 or 2 column

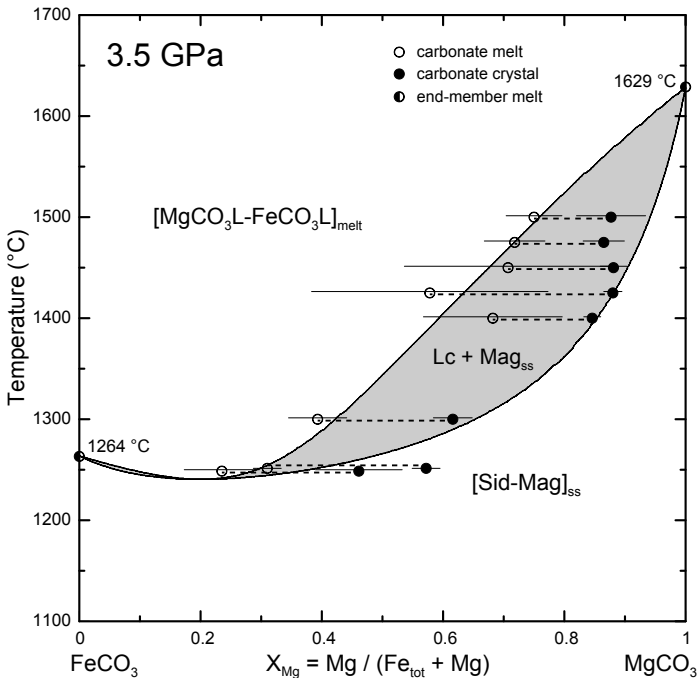


Fig. 4
1 column

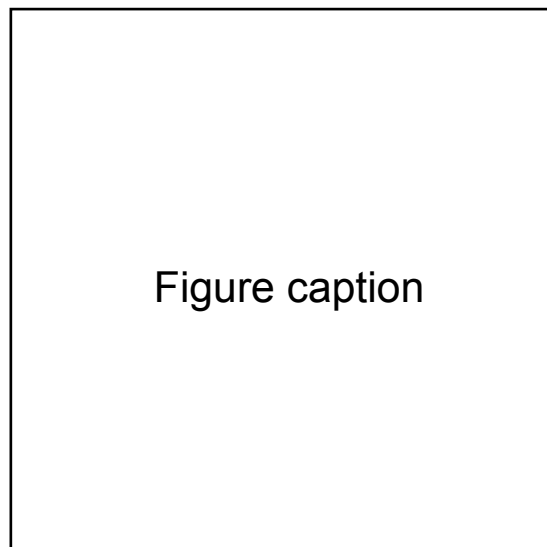
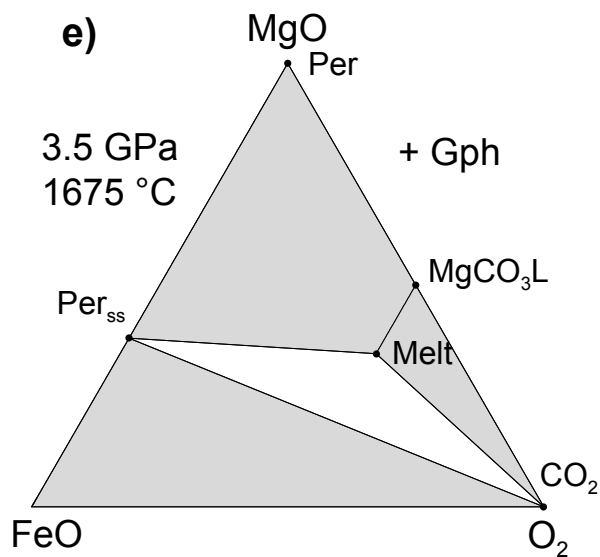
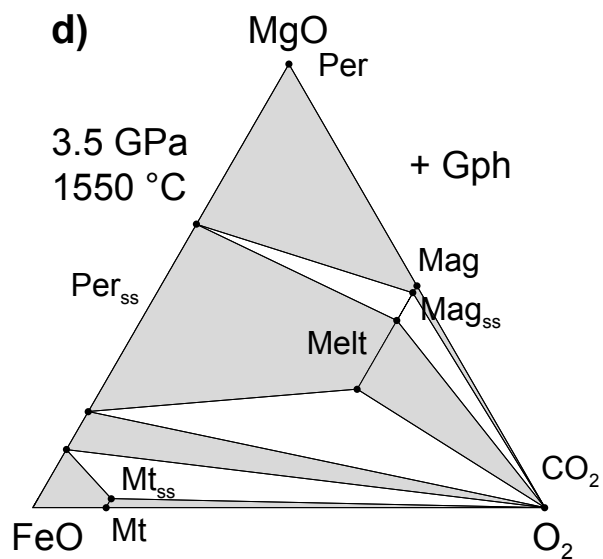
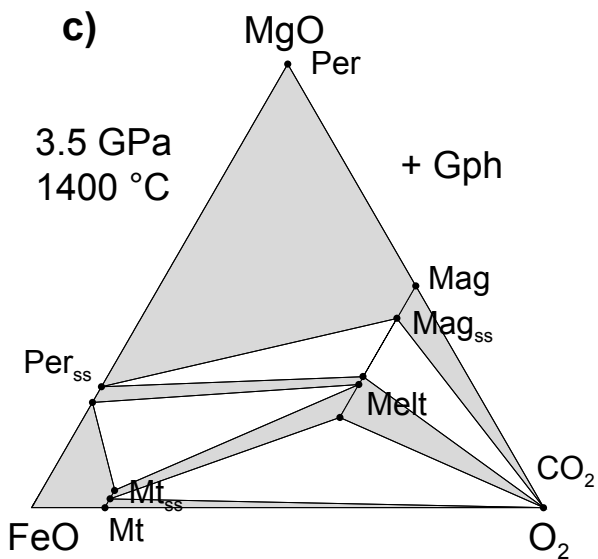
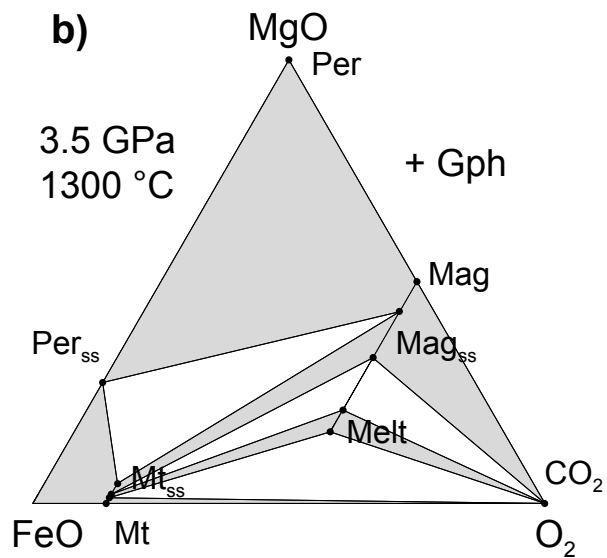
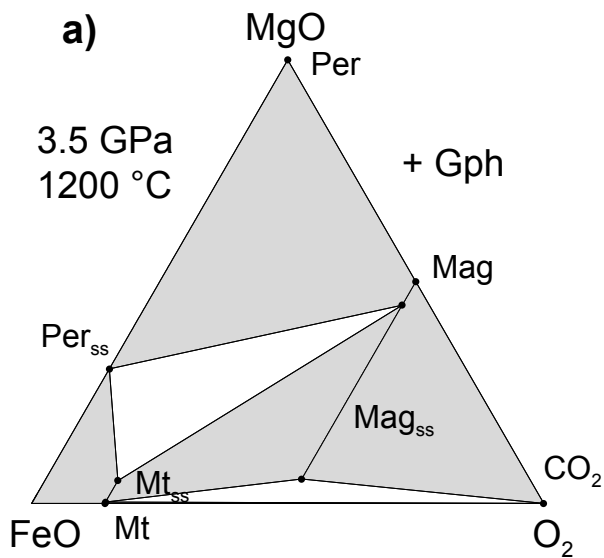


Fig. 5
1.5 or 2 column

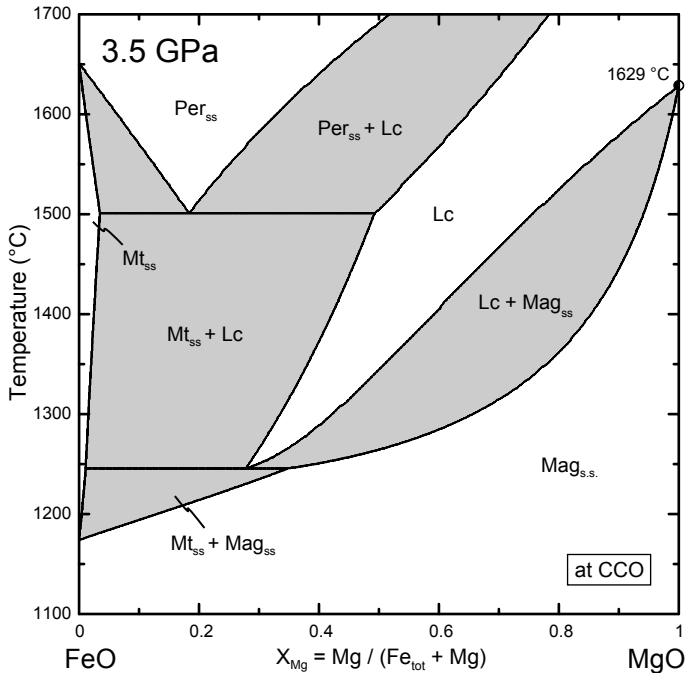


Fig. 6
1 column

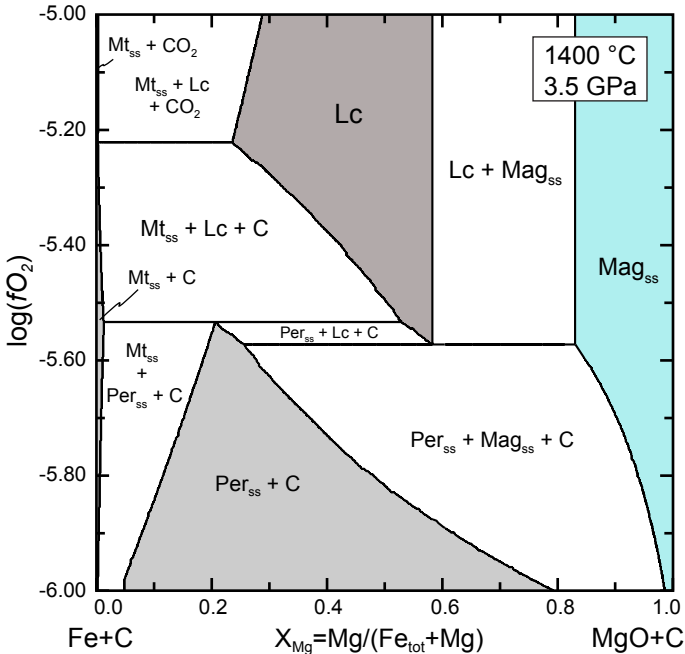


Fig. 7
 1 column

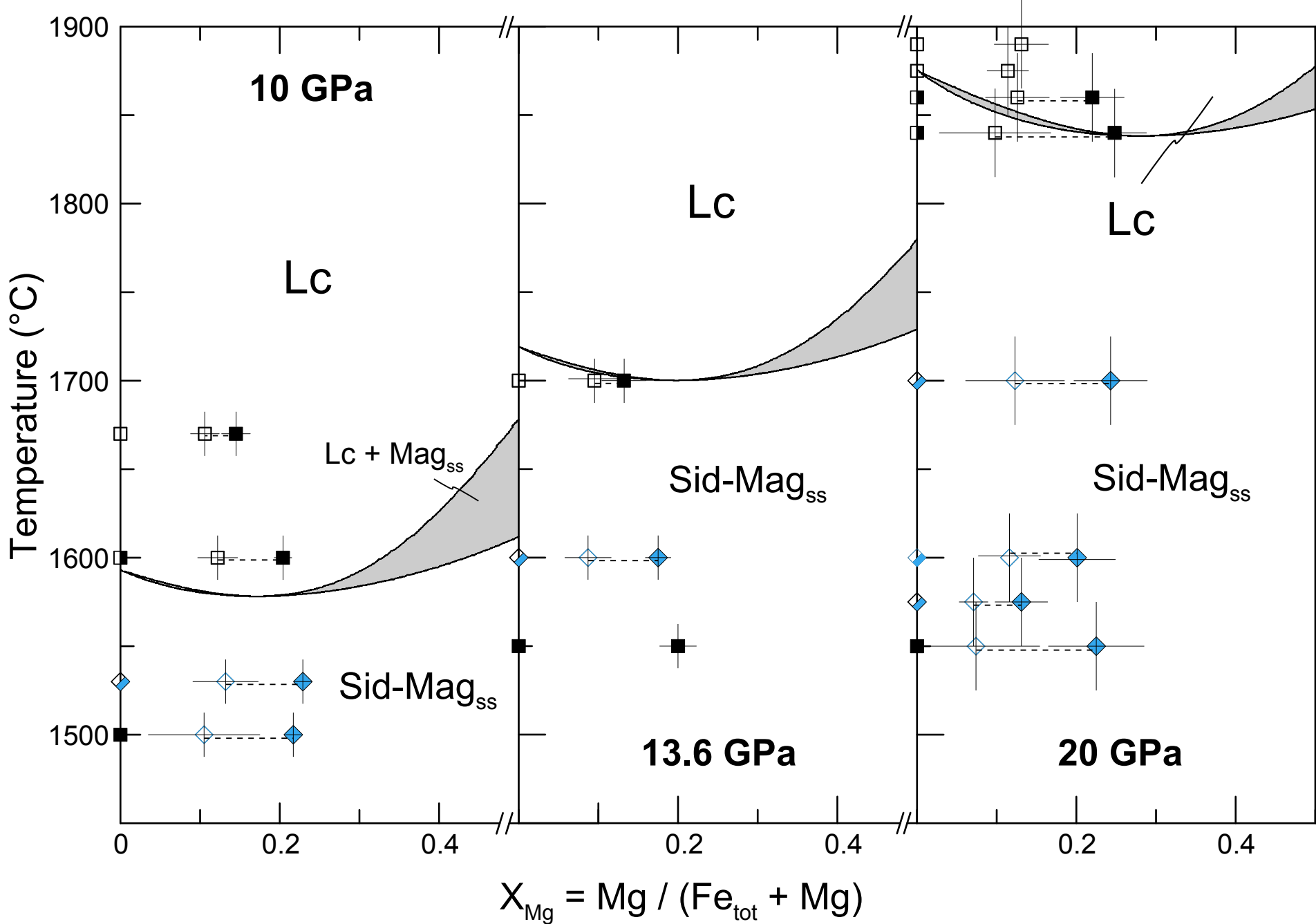


Fig. 8
1.5 or 2 column